Title	Time-Dependent Long-Range-Corrected Density-Functional Tight-Binding Method Combined with the Polarizable Continuum Model
Author(s)	Nishimoto, Yoshio
Citation	Journal of Physical Chemistry A (2019), 123(26): 5649-5659
Issue Date	2019-07-05
URL	http://hdl.handle.net/2433/243214
Right	This document is the unedited author's version of a Submitted Work that was subsequently accepted for publication in Journal of Physical Chemistry A, copyright © American Chemical Society after peer review. To access the final edited and published work, see https://doi.org/10.1021/acs.jpca.9b03713.; The full-text file will be made open to the public on 31 May 2020 in accordance with publisher's 'Terms and Conditions for Self-Archiving'.; This is not the published version. Please cite only the published version. この論文は出版社版でありません。引用の際には出版社版をご確認ご利用ください。
Type	Journal Article
Textversion	author

Time-Dependent Long-Range Corrected Density-Functional Tight-Binding Method Combined with the Polarizable Continuum Model

Yoshio Nishimoto*

Fukui Institute for Fundamental Chemistry, Kyoto University, 34-4 Takano Nishihiraki-cho, Sakyo-ku, Kyoto 606-8103, Japan

E-mail: nishimoto.yoshio@fukui.kyoto-u.ac.jp

Phone: +81 (0)75 711-7894

Abstract

In this study, excited-state free energies and geometries were efficiently evaluated using a linear-response time-dependent long-range corrected density-functional tight-binding method integrated with the polarizable continuum model (TD-LC-DFTB2/PCM). Although the LC-DFTB method required the evaluation of the exchange-type term, which was moderately computationally expensive, a single evaluation of the excited-state gradient for a system consisting of more than 1000 atoms in a vacuum was completed within 30 minutes using one CPU core. Benchmark calculations were conducted for 3-hydroxyflavone, which exhibits dual emission: the absorption and enol-form emission wavelengths calculated by TD-LC-DFTB2/PCM agreed well with those predicted based on density functional theory using a long-range corrected functional; however, there was a large error in the predicted keto-form emission wavelength. Further benchmark calculations for more than 20 molecules indicated that the conventional TD-DFTB method underestimated the absorption and 0–0 transition energies compared with those which were measured experimentally while the TD-LC-DFTB2 method systematically overestimated these metrics. Nevertheless, the agreement of the results of the TD-LC-DFTB2 method with those obtained by the CAM-B3LYP method demonstrates the potential of the TD-LC-DFTB2/PCM method. Moreover, changing the range-separation parameter to 0.15 minimized this deviation.

INTRODUCTION

The development of large-scale quantum mechanical (QM) methods[1] is one of the hottest topics in computational chemistry. These methods can be used to evaluate large systems and obtain large numbers of samples in molecular dynamics simulations. Standard single-reference QM methods, such as Hartree–Fock and density functional theory (DFT), are much more economical than electron correlation methods but are still rather time-consuming; thus, it is difficult to evaluate large systems using these techniques. In the standard implementation of Hartree–Fock and DFT, the bottleneck is sometimes the evaluation of the two-electron

integrals or, in DFT, exchange–correlation contributions. This bottleneck can be alleviated by employing screening techniques[2] but routine calculations for systems comprising more than one thousand atoms is still prohibitively expensive without linear scaling techniques unless significant computational resources are available.[1] Modeling excited states is even more computationally demanding; the linear-response time-dependent DFT (TD-DFT) for systems consisting of only a few hundred atoms is already challenging.

QM methods can be drastically simplified by applying various approximations or employing fitted parameters, giving rise to semi-empirical QM methods. For instance, the self-consistent charge density-functional tight-binding (DFTB) method[3] was derived by introducing tight-binding approximations and applying a Taylor expansion to the density fluctuation of DFT. Depending on the order of the Taylor expansion, the conventional DFTB method is sometimes referred to as DFTB2[3] and DFTB3[4] for second- and third-order expansions, respectively. As the derived expression contains multiple parameters, DFTB is expected to be two or three orders of magnitude faster than DFT with comparable accuracy when applied with generalized gradient approximation (GGA) functionals. DFTB was first applied to calculate excited states in the framework of the linear-response time-dependent approach (TD-DFTB) by Niehaus et al.[5] More recently, an analytic derivative of TD-DFTB using the Z-vector method[6] was derived and implemented.[7] As the TD-DFTB method is very fast, it has been applied to systems consisting of more than one thousand atoms.[8–12] However, it is widely known that the accuracy of TD-DFTB is rather limited, particularly for charge-transfer excitations, as DFT with GGA functionals exhibits a similar difficulty.

As in many semi-empirical QM methods, DFTB had been missing exchange-type contributions until very recently, when long-range corrected DFTB (namely, LC-DFTB) was proposed by two research groups.[13–15] LC-DFTB was first presented in a seminal work by Niehaus et al.,[13] which mainly proposed and formalized the method based on a Yukawa-type exchange interaction of a homogeneous electron gas. LC-DFTB was first implemented, including an extension to linear-response time-dependent calculations (lc-TD-DFTB; here

referred to as TD-LC-DFTB), by Humeniuk et al. in 2015[14] and later implemented for ground state calculations by Lutsker et al. in the same year.[15] Different definitions for the exchange-type contributions had been used in these two studies. In 2017, Humeniuk et al., however, modified the formulation[16] to use the difference density matrix, making it similar to the other formulation although the two formulations split the inverse distance differently (refs 13 and 15 employ an exponential function, whereas refs 14 and 16 use the error function). In terms of the formulation, the major difference between LC-DFTB and conventional DFTB is that the former involves exchange-type contributions. All previous linear-response TD-LC-DFTB studies[14,16–18] have reported that the prediction of excitation energies is improved compared to that with the conventional TD-DFTB2, particularly for charge-transfer excitations. However, few of these studies employed analytic geometrical derivatives of TD-LC-DFTB.[16]

To evaluate the excited-state properties of molecules in solution, a QM method is commonly combined with an implicit solvent model because of the low computational cost and reasonable accuracy of such models in describing solvent effects. Perhaps the most well-known of these models is the polarizable continuum model (PCM),[19] which was integrated with DFTB, extended to TD-DFTB, and implemented in Gaussian by Barone et al.[20] Later, analytic derivatives of TD-DFTB with PCM, namely, TD-DFTB/PCM, were realized[11] in the General Atomic and Molecular Electronic Structure System, United States (GAMESS-US).[21] Very recently, LC-DFTB2 was implemented in the GAMESS-US package and combined with the fragment molecular orbital method[22] to carry out calculations for systems as large as 9984 atoms. In all of the aforementioned TD-LC-DFTB studies, the calculations were performed under the assumption of a vacuum; TD-LC-DFTB could not be applied to study excited-state properties in solution unless explicit solvent molecules were added.

In this study, we develop a novel TD-LC-DFTB2/PCM approach based on the previous implementation in GAMESS-US.[22] In one of the initial implementations of the ground-state LC-DFTB,[15] it was reported that the computational cost of LC-DFTB was roughly ten

times higher than that of the conventional DFTB; hence, an integral-screening technique was utilized. In another implementation, the "active space" technique is utilized in the computation of excited-state energies.[16] Considering these approximations, the additional cost associated with the evaluation of the exchange-type contribution in LC-DFTB prevents its application to larger systems; thus, it is important to compute this term efficiently. Herein, we assess the performance of three TD-DFTB models, namely TD-DFTB2,[13] TD-DFTB3,[23] and TD-LC-DFTB2, in terms of the absorption and 0–0 transition energies predicted for selected molecules relative to those in the benchmark set by Jacquemin et al.[24]

METHODOLOGY

In this section, i and j denote occupied molecular orbitals (MOs), a and b denote virtual MOs, and p, q, r, and s denote general MOs. μ, ν, κ, and λ represent the atomic orbitals (AOs) in atoms A, B, C, and D, respectively. σ and τ represent the electron spins of different atoms. $\delta_{\sigma\tau}$ stands for the Kronecker delta, which is one when $\sigma = \tau$ and zero when $\sigma \neq \tau$.

Overview of LC-DFTB2/PCM

Following the formulation proposed by Lutsker et al.,[15] the total energy of LC-DFTB2 (without PCM) can be written as follows:

$$E = \sum_{\mu\nu}\sum_{\sigma} D_{\mu\nu\sigma} H^0_{\mu\nu} + \frac{1}{2}\sum_{AB} \gamma_{AB} \Delta Q_A \Delta Q_B + E^{\mathrm{rep}} - \frac{1}{2}\sum_{\mu\nu\kappa\lambda}\sum_{\sigma} (\mu\kappa|\nu\lambda)^{\mathrm{lr}} \Delta D_{\mu\nu\sigma} \Delta D_{\kappa\lambda\sigma} \ . \quad (1)$$

If the last term is omitted, the apparent expression is equivalent to the conventional second-order DFTB (DFTB2). The density matrix is defined as follows:

$$D_{\mu\nu\sigma} = \sum_i f_{i\sigma} C_{\mu i\sigma} C^*_{\nu i\sigma} \ , \quad (2)$$

where $f_{i\sigma} = 1$ is the orbital occupation number of the ith MO in σ spin and $C_{\mu i\sigma}$ is the standard MO coefficient matrix. It is assumed that $\mathbf{C} = \mathbf{C}^*$ in this study. The zeroth-order Hamiltonian, $H^0_{\mu\nu}$, contains kinetic, nuclear–electron, electron–electron, and exchange–correlation contributions from the reference (unperturbed) electron density and is computed by interpolating the parameter (Slater–Koster) files. The function γ_{AB}, which depends on the distance between two atoms (r_{AB}) and their Hubbard values (which are related to the chemical hardness[25]), describes the Coulombic and full-range exchange–correlation contributions. It asymptotically converges to the inverse of the distance between the two atoms when this distance is sufficiently long. The atom-resolved Mulliken charge, ΔQ_A, is obtained as the difference between the atom-resolved Mulliken population, Q_A,

$$Q_A = \sum_{\mu\in A}\sum_{\nu}\sum_{\sigma} D_{\mu\nu\sigma} S_{\mu\nu} \ , \tag{3}$$

where $S_{\mu\nu}$ is the overlap matrix, and the number of valence electrons on the neutral atom A, Q^0_A (i.e., $\Delta Q_A = Q_A - Q^0_A$). E^{rep} is the sum of the repulsive potentials between all unique pairs of atoms.

The last term in eq 1 is newly added to LC-DFTB. The difference density matrix, $\Delta D_{\mu\nu}$, is defined as the difference between the standard density matrix (eq 2) and the reference density matrix, $D^0_{\mu\nu}$ (i.e., $\Delta D_{\mu\nu} = D_{\mu\nu} - D^0_{\mu\nu}$). The reference density matrix is a diagonal matrix containing the number of valence electrons of the free neutral atoms in each AO. The four-index exchange-type integral, $(\mu\kappa|\nu\lambda)^{\mathrm{lr}}$, is defined as follows

$$(\mu\kappa|\nu\lambda)^{\mathrm{lr}} = \frac{1}{4} S_{\mu\kappa} S_{\nu\lambda} \left(\gamma^{\mathrm{lr}}_{AB} + \gamma^{\mathrm{lr}}_{AD} + \gamma^{\mathrm{lr}}_{CB} + \gamma^{\mathrm{lr}}_{CD}\right) \ . \tag{4}$$

The atom-resolved long-range function, $\gamma^{\mathrm{lr}}_{AB}$, is defined as in ref 15 and computed analytically. In addition to depending on r_{AB} and the Hubbard values of these atoms, $\gamma^{\mathrm{lr}}_{AB}$ now additionally depends on the range-separation parameter ω as in the long-range corrected DFT.

With PCM, the above energy is sometimes referred to as the internal energy of the solute.

The total free energy of the solute–solvent system $\mathcal{G}$ can be expressed as

$$\mathcal{G} = E + \frac{1}{2}E^{\mathrm{int}} + \mathcal{G}^{\mathrm{cdr}} \ , \tag{5}$$

where E^{int} represents the electrostatic interaction between the solute and solvent and $\mathcal{G}^{\mathrm{cdr}}$ represents the sum of the non-electrostatic cavitation, dispersion, and repulsive free energies. Note that eq 5 is the free energy of the solute–solvent system. The half of E^{int} is spent to polarize the dielectric medium when a molecule is inserted into a cavity. A more detailed discussion may be found in ref 19. Within the DFTB/PCM employed in this study, E^{int} is defined as follows:[11]

$$E^{\mathrm{int}} = -\sum_{A} \Delta Q_A \sum_{k}^{N_{\mathrm{ts}}} \frac{\bar{q}_k}{r_{Ak}} \ , \tag{6}$$

where $\bar{q}_k$ is the induced surface charge of the kth tessera, N_{ts} is the number of tesserae, and r_{Ak} is the distance between atom A and tessera k (tesserae are discretized surface elements of the solute–solvent interface). Induced charges or apparent surface charges are obtained by solving the following matrix equation:

$$\bar{\mathbf{q}} = -\bar{\mathbf{C}}^{-1}\bar{\mathbf{v}} \ , \tag{7}$$

where $\bar{\mathbf{C}}$ is a matrix that depends on the positions of the tesserae and the PCM model that is selected. In this study, conductor PCM[26] is employed, and the prefactor of $\varepsilon/(\varepsilon - 1)$, where ε is the dielectric constant of the solvent, is included in $\bar{\mathbf{C}}$ for simplicity. $\bar{\mathbf{v}}$ is the electrostatic potential on the kth tessera and, in the present implementation, is defined by

$$\bar{v}_k = -\sum_{A} \frac{\Delta Q_A}{r_{Ak}} \ . \tag{8}$$

In LC-DFTB2/PCM, the Hamiltonian can be expressed as

$$H_{\mu\nu\sigma} = H^0_{\mu\nu} + \sum_{\kappa\lambda\tau} \left\{ (\mu\nu|\kappa\lambda) - \delta_{\sigma\tau} \left(\mu\kappa|\lambda\nu\right)^{\mathrm{lr}} + G_{\mu\nu,\kappa\lambda} \right\} \Delta D_{\kappa\lambda\tau} \ , \tag{9}$$

where the full-range two-electron integral and the PCM contribution[20] in the AO representation are

$$(\mu\nu|\kappa\lambda) = \frac{1}{4} S_{\mu\nu} S_{\kappa\lambda} \left(\gamma_{AB} + \gamma_{AD} + \gamma_{CB} + \gamma_{CD}\right) \tag{10}$$

and

$$G_{\mu\nu,\kappa\lambda} = -\frac{1}{4} S_{\mu\nu} S_{\kappa\lambda} \sum_{kl}^{N_{\mathrm{ts}}} \left(\frac{1}{r_{Ak}} + \frac{1}{r_{Bk}}\right) \left(\bar{\mathbf{C}}^{-1}\right)_{kl} \left(\frac{1}{r_{Cl}} + \frac{1}{r_{Dl}}\right) \ , \tag{11}$$

respectively. Clearly, the LC-DFTB2 Hamiltonian in a vacuum can be obtained by omitting the $G_{\mu\nu,\kappa\lambda}$ term.

By differentiating the total free energy with respect to a geometrical parameter x, its first-order derivative for the ground state is obtained as follows:

$$\begin{aligned}
\frac{\mathrm{d}\mathcal{G}}{\mathrm{d}x} = & \sum_i \sum_\sigma f_{i\sigma} \sum_{\mu\nu} C_{\mu i\sigma} C_{\nu i\sigma} \left[\frac{\partial H^0_{\mu\nu}}{\partial x} - \varepsilon_{i\sigma} \frac{\partial S_{\mu\nu}}{\partial x} \right. \\
& \left. + \frac{1}{2} \frac{\partial S_{\mu\nu}}{\partial x} \left\{ \sum_C \left(\gamma_{AC} + \gamma_{BC}\right) \Delta Q_C - \sum_k^{N_{\mathrm{ts}}} \left(\frac{1}{r_{Ak}} + \frac{1}{r_{Bk}}\right) \bar{q}_k \right\} \right] \\
& + \frac{1}{2} \sum_{AB} \frac{\partial \gamma_{AB}}{\partial x} \Delta q_A \Delta q_B - \frac{1}{2} \sum_{\mu\nu\kappa\lambda} \sum_\sigma \frac{\partial \left(\mu\kappa|\nu\lambda\right)^{\mathrm{lr}}}{\partial x} \Delta D_{\mu\nu\sigma} \Delta D_{\kappa\lambda\sigma} \\
& + \frac{\partial E^{\mathrm{rep}}}{\partial x} - \sum_A \Delta Q_A \sum_k^{N_{\mathrm{ts}}} \bar{q}_k \frac{\partial r^{-1}_{Ak}}{\partial x} + \frac{1}{2} \bar{\mathbf{q}}^{\mathrm{T}} \frac{\partial \bar{\mathbf{C}}}{\partial x} \bar{\mathbf{q}} + \frac{\partial \mathcal{G}^{\mathrm{cdr}}}{\partial x} \ ,
\end{aligned} \tag{12}$$

where $\varepsilon_{i\sigma}$ is the eigenvalue of the ith MO. It should be noted that displacements of the tesserae have to be included in the actual calculation and this contribution is implicitly included in the $\partial r^{-1}_{Ak}/\partial x$ term. The third term is newly added in LC-DFTB/PCM; the computation of this term is discussed in the Supporting Information.

The excitation energies, Ω, and excitation and deexcitation vectors, $\mathbf{X}$ and $\mathbf{Y}$, respec-

tively, can be obtained by solving the following non-Hermitian equation:

$$\begin{pmatrix} \mathbf{A} & \mathbf{B} \\ \mathbf{B} & \mathbf{A} \end{pmatrix} \begin{pmatrix} \mathbf{X} \\ \mathbf{Y} \end{pmatrix} = \Omega \begin{pmatrix} \mathbf{1} & \mathbf{0} \\ \mathbf{0} & -\mathbf{1} \end{pmatrix} \begin{pmatrix} \mathbf{X} \\ \mathbf{Y} \end{pmatrix} \ , \tag{13}$$

where the matrix elements of $\mathbf{A}$ and $\mathbf{B}$ are defined as

$$A_{ia\sigma,jb\tau} = \delta_{ij}\delta_{ab}\delta_{\sigma\tau}(\varepsilon_{a\sigma} - \varepsilon_{i\sigma}) + K_{ia\sigma,jb\tau} + G_{ia\sigma,jb\tau} \tag{14}$$

and

$$B_{ia\sigma,jb\tau} = K_{ia\sigma,bj\tau} + G_{ia\sigma,bj\tau} \ . \tag{15}$$

The coupling matrix, $K_{ia\sigma,jb\tau}$, for singlet–singlet excitation is defined by

$$K_{pq\sigma,rs\tau} = (pq\sigma|rs\tau) - \delta_{\sigma\tau}\left(pr\sigma|qs\tau\right)^{\mathrm{lr}} \tag{16}$$

For singlet–triplet excitation, the first term in eq 16 is replaced with spin constant matrix elements.[5,23] In eq 16, eqs 10 and 4 are transformed to an MO representation. For instance,

$$(pq\sigma|rs\tau) = \sum_{\mu\nu\rho\sigma} C_{\mu p\sigma}C_{\nu q\sigma}C_{\kappa r\tau}C_{\lambda s\tau}\left(\mu\nu|\kappa\lambda\right) \ . \tag{17}$$

The PCM contribution $G_{ia\sigma,jb\tau}$ is given by

$$G_{pq\sigma,rs\tau} = -\sum_{A} Q_A^{pq\sigma} \sum_{k}^{N_{\mathrm{ts}}} \frac{\bar{q}_k^{rs\tau}}{r_{Ak}} \ , \tag{18}$$

where $\bar{q}_k^{rs\tau}$ is the induced charge obtained by solving eq 7 with the potentials on the tesserae:

$$\bar{v}_k^{rs\tau} = -\sum_{A} \frac{Q_A^{rs\tau}}{r_{Ak}} \ , \tag{19}$$

where

$$Q_A^{rs\tau} = \frac{1}{2} \sum_{\mu \in A} \sum_{\nu} \left(C_{\mu r \tau} C_{\nu s \tau} + C_{\mu s \tau} C_{\nu r \tau} \right) S_{\mu \nu} \ . \tag{20}$$

In practice, $G_{ia\sigma,jb\tau}$ is not constructed or stored; instead, the matrix–vector product is taken as follows:

$$\begin{aligned} \sum_{jb\tau} G_{ia\sigma,jb\tau} b_{jb\tau} &= \sum_{\mu\nu\kappa\lambda} \sum_{\tau} C_{\mu i \sigma} C_{\nu a \sigma} G_{\mu\nu,\kappa\lambda} \left(\sum_{jb} C_{\kappa j \tau} C_{\lambda b \tau} b_{jb\tau} \right) \\ &= \sum_{\mu\nu\kappa\lambda} \sum_{\tau} C_{\mu i \sigma} C_{\nu a \sigma} G_{\mu\nu,\kappa\lambda} D'_{\kappa\lambda\tau} \ , \end{aligned} \tag{21}$$

where $b_{jb\tau}$ is the trial vector and $D'_{\kappa\lambda\tau}$ is a density-like matrix. Here, $D'_{\kappa\lambda\tau}$ is calculated as described previously by:[27]

$$D'_{\mu\nu\tau} = \sum_{jb} C_{\mu j \tau} C_{\nu b \tau} b_{jb\tau} \ , \tag{22}$$

which is not necessarily symmetric.

Analytic gradient for TD-LC-DFTB2/PCM

Analytic derivatives of TD-LC-DFTB2 were first developed and implemented in 2017 by Humeniuk et al.[16] They were derived by applying the Z-vector method in a similar way to those described in previous studies,[6,28] which is common in TD-DFT. As the necessary expressions are already given in ref 16, the details are not presented here; however, some expressions must be reviewed to prepare for the integration of TD-LC-DFTB2 with PCM. Analytic derivatives of TD-DFT/PCM were previously described in refs 29 and 30.

Because the excitation energy within TD-DFTB is not stationary with respect to any changes in $C_{\mu i}$, the response contributions must be evaluated to compute the first-order derivatives analytically. Instead of solving a large number ($3 \times N_{\mathrm{at}}$, where N_{at} is the number of atoms in the system) of coupled-perturbed equations, the Z-vector method[6] is usually

employed so only one linear matrix equation must be solved:

$$\sum_{jb\tau} \left(\mathbf{A}+\mathbf{B}\right)_{ia\sigma,jb\tau} Z_{jb\tau} = -R_{ia\sigma} \ , \tag{23}$$

where

$$\begin{aligned} R_{ia\sigma} = & \sum_{b} \left\{ \left(\mathbf{X}+\mathbf{Y}\right)_{ib\sigma} H^{+}_{ab\sigma}[(\mathbf{X}+\mathbf{Y})] + \left(\mathbf{X}-\mathbf{Y}\right)_{ib\sigma} H^{-}_{ab\sigma}[(\mathbf{X}-\mathbf{Y})] \right\} \\ & - \sum_{j} \left\{ \left(\mathbf{X}+\mathbf{Y}\right)_{ja\sigma} H^{+}_{ji\sigma}[(\mathbf{X}+\mathbf{Y})] + \left(\mathbf{X}-\mathbf{Y}\right)_{ja\sigma} H^{-}_{ji\sigma}[(\mathbf{X}-\mathbf{Y})] \right\} \\ & + H^{+}_{ia\sigma}[\mathbf{T}] \ . \end{aligned} \tag{24}$$

The unrelaxed difference density matrix $\mathbf{T}$ is defined elsewhere;[28,31] for an arbitrary vector or matrix $\mathbf{V}$,

$$\begin{aligned} H^{+}_{pq\sigma}[\mathbf{V}] &= \sum_{rs\tau} \left(K_{pq\sigma,rs\tau} + G_{pq\sigma,rs\tau} + K_{pq\sigma,sr\tau} + G_{pq\sigma,sr\tau}\right) V_{rs\tau} \\ &= \sum_{rs\tau} \left(2\left(pq\sigma|rs\tau\right) - \delta_{\sigma\tau} \left\{ \left(pr\sigma|qs\tau\right)^{\mathrm{lr}} + \left(ps\sigma|qr\tau\right)^{\mathrm{lr}} \right\} + 2G_{pq\sigma,rs\tau} \right) V_{rs\tau} \end{aligned} \tag{25}$$

and

$$\begin{aligned} H^{-}_{pq\sigma}[\mathbf{V}] &= \sum_{rs\tau} \left(K_{pq\sigma,rs\tau} - K_{pq\sigma,sr\tau}\right) V_{rs\tau} \\ &= -\sum_{rs\tau} \delta_{\sigma\tau} \left\{ \left(pr\sigma|qs\tau\right)^{\mathrm{lr}} - \left(ps\sigma|qr\tau\right)^{\mathrm{lr}} \right\} V_{rs\tau} \ . \end{aligned} \tag{26}$$

In the previous TD-DFTB/PCM implementation,[11] $H^{-}_{pq\sigma}[\mathbf{V}]$ was always zero because long-range corrections were not yet introduced. Compared with the TD-LC-DFTB2 in a vacuum,[16] an additional evaluation of the $G_{pq\sigma,rs\tau}$ in $H^{+}_{pq\sigma}[\mathbf{V}]$ term is required for the combination with PCM.

Once the Z-vector equation has been solved self-consistently, the relaxed one-particle difference density matrix ($\mathbf{P} = \mathbf{T} + \mathbf{Z}$) and a Lagrange multiplier vector ($\mathbf{W}$; the energy-weighted difference density matrix) can be constructed according to the definitions in refs 28 and 31. After transforming the vectors defined in the MO representation to those in the AO representation (as in eq 22), the first-order derivative of the excitation energy can be determined as follows:

$$\begin{aligned}\frac{\mathrm{d}\Omega}{\mathrm{d}x} = &\sum_{\mu\nu\sigma} \frac{\partial H^0_{\mu\nu}}{\partial x} P_{\mu\nu\sigma} - \sum_{\mu\nu\sigma} \frac{\partial S_{\mu\nu}}{\partial x} W_{\mu\nu\sigma} + \sum_{\mu\nu\sigma\kappa\lambda\tau} \frac{\partial \left(\mu\nu|\kappa\lambda\right)}{\partial x} \mathit{\Gamma}_{\mu\nu\sigma,\kappa\lambda\tau} \\ &+ \sum_{\mu\nu\sigma\kappa\lambda\tau} \frac{\partial \left(\mu\nu|\kappa\lambda\right)^{\mathrm{lr}}}{\partial x} \mathit{\Gamma}^{\mathrm{ex}}_{\mu\nu\sigma,\kappa\lambda\tau} + \sum_{\mu\nu\sigma\kappa\lambda\tau} \frac{\partial G_{\mu\nu,\kappa\lambda}}{\partial x} \mathit{\Gamma}_{\mu\nu\sigma,\kappa\lambda\tau} \ , \end{aligned} \tag{27}$$

where the two-particle difference density matrix has been divided into two contributions: that of the Coulomb-type integrals,

$$\mathit{\Gamma}_{\mu\nu\sigma,\kappa\lambda\tau} = P_{\mu\nu\sigma} D_{\kappa\lambda\tau} + \left(\mathbf{X}+\mathbf{Y}\right)_{\mu\nu\sigma} \left(\mathbf{X}+\mathbf{Y}\right)_{\kappa\lambda\tau} \tag{28}$$

and that of the exchange-type integrals,

$$\begin{aligned}\mathit{\Gamma}^{\mathrm{ex}}_{\mu\nu\sigma,\kappa\lambda\tau} = -\frac{\delta_{\sigma\tau}}{2}\Big(&P_{\mu\kappa\sigma} D_{\nu\lambda\tau} + P_{\mu\lambda} D_{\nu\kappa\tau} \\ &+ \left(\mathbf{X}+\mathbf{Y}\right)_{\mu\kappa\sigma} \left(\mathbf{X}+\mathbf{Y}\right)_{\nu\lambda\tau} + \left(\mathbf{X}+\mathbf{Y}\right)_{\mu\kappa\sigma} \left(\mathbf{X}+\mathbf{Y}\right)_{\lambda\nu\tau} \\ &+ \left(\mathbf{X}-\mathbf{Y}\right)_{\mu\kappa\sigma} \left(\mathbf{X}-\mathbf{Y}\right)_{\nu\lambda\tau} - \left(\mathbf{X}-\mathbf{Y}\right)_{\mu\kappa\sigma} \left(\mathbf{X}-\mathbf{Y}\right)_{\lambda\nu\tau}\Big) \ . \end{aligned} \tag{29}$$

The explicit PCM contribution (i.e., the last term in eq 27, is identical to that presented in eq 25 in ref 11 and comes from only the two-particle difference density matrix for Coulomb-type integrals ($(\mathbf{X}-\mathbf{Y})$ contributions are not involved in in the explicit PCM contribution).

Implementation of TD-LC-DFTB2

TD-LC-DFTB2/PCM was implemented in GAMESS-US[21] on top of the previous implementation of LC-DFTB2.[22] In this implementation, it is possible to employ the Tamm–Dancoff approximation[32] by neglecting the deexcitation vector, $\mathbf{Y}$. In TD-LC-DFTB2/PCM, if the numerical gradients are computed carefully, the differences between the analytic and numerical gradients in the excited states are on the order of 10^{-7} hartree/bohr.

As stated previously, calculating the exchange contribution incurs a high computational cost. One solution is to employ a Schwarz-like screening as in ref 15; however, this approach may require the threshold to be chosen carefully or the overhead associated with the screening process can be heavy. In particular, the efficiency of the algorithm depends heavily on the shape of the molecule. For example, if the system is linear, the overlap and density matrices are very sparse so the screening approach reduces the number of matrix elements that are evaluated significantly; in contrast, if the system is condensed and/or three-dimensional, this effect may not be significant. When the system is charged, $\Delta D_{\mu\nu}$ tends to be less sparse. Hence, in the present implementation in GAMESS-US, the direct computation approach that was adopted in ref 14 was employed.

The derivation of working equations is rather lengthy and technical, so mathematical expressions are given in the Supporting Information. The expressions herein show that the entire exchange-type contribution to the gradient in LC-DFTB2 can be computed with $\mathcal{O}\left(N_{\mathrm{AO}}^3\right)$ complexity, where N_{AO} is the number of AOs. These expressions also imply that it is possible for large systems to benefit from sparse matrix multiplications.

COMPUTATIONAL DETAILS

In the following calculations, the MIO,[3,33,34] 3OB,[35–37] and OB2(base)[38] parameter sets were employed for the DFTB2, DFTB3, and LC-DFTB2 calculations, respectively. In the LC-DFTB2 calculation, the range-separation parameter ω must be specified. In principle, this

parameter is intrinsic to the OB2 parameter set. Therefore, $\omega = 0.30$, as specified in ref 38, is used for all calculations unless otherwise noted. There are other two variants of the OB2 parameter set: shift and split. These two sets are developed mainly to balance the nitrogen's sp^2 and sp^3 hybridization.[38] Preliminary calculations for pyridine indicate that the difference of the first excitation energy is no more than 0.03 eV, so the different parameter set should not affect the result significantly. Most of the computational setup, such as the convergence criteria and PCM-related parameters, was the same as that in ref 11; however, in contrast, no dispersion corrections were included in the following calculations unless otherwise noted. Second-order geometrical derivatives were computed by a finite difference method using analytic first-order geometrical derivatives with a step size of 5.0×10^{-3} a.u.

First, the computational efficiency of (TD-)DFTB2 and (TD-)LC-DFTB2 using one CPU core (Xeon E5-1650 v3) was benchmarked with a series of *trans*-polyacetylene chains ($C_{50n}H_{50n+2}$; $n = 4, 5, \ldots, 10$); smaller chains ($n = 1$, 2, and 3) were excluded because the computation time was negligibly short for these molecules. Only the CPU times are presented as the wall-clock time was almost identical to the CPU times since the CPU utilization was always above 99% for these molecules. The ten lowest excitation energies were computed during the excited-state calculations. The analytic gradient at the first singlet excited state (S_1) was also computed.

Next, the accuracy of the implemented method was benchmarked with a molecule that exhibits dual emission, 3-hydroxyflavone (3HF), as in a previous study.[11] The computational setup was identical to that in the previous study. In the present study, the corrected linear-response (cLR) solvation model[39] was employed to evaluate the absorption and emission energies. The absorption energy can be directly determined from the excitation energy using the linear-response (LR) solvation approach, which is widely employed in excited-state calculations in a solution phase. Alternatively, it can be determined as the difference between the free energies of the excited and ground states using the cLR and state-specific (SS)[40] approaches; consequently, the free energies of the excited states must be defined and

computed using the cLR and SS approaches such that they are comparable with the ground state, which necessitates the computation of the relaxed density in the excited state ($\mathbf{P}$) by solving the Z-vector equation. The cLR and SS approaches differ in the self-consistency of the reaction field.[39] A similar procedure can be applied to compute the emission energy. The necessary equations were derived and implemented based on ref 39. The absorption and emission energies were computed with the non-equilibrium cLR solvation model, but the geometry optimizations were performed with the equilibrium LR solvation model as usual.

Finally, to further evaluate the performance of TD-LC-DFTB2/PCM, benchmark calculations were performed using TD-DFTB2, TD-DFTB3, and TD-LC-DFTB2 combined with the cLR-PCM approach for the molecular set proposed in ref 24. Since the experimental data listed in ref 24 was obtained in a solution phase, it is important to properly consider the solvent effects. The 0–0 transition energies within non-equilibrium cLR-PCM were computed following the procedure outlined in ref 24; the initial geometries were also taken from this source. Because of the limited availability of DFTB (Slater–Koster) parameters, 35 molecules could be calculated by TD-DFTB2 and TD-DFTB3 and 25 molecules could be calculated by TD-LC-DFTB2. The statistical comparisons between methods were done based on the latter 25 molecules (or 24 for the comparisons of calculated 0–0 transition energies). The threshold for the geometry convergence was raised to 10^{-5} hartree/bohr for a few cases. The calculated absorptions and 0–0 transition energies are summarized in the Supporting Information (Tables S1 and S2).

RESULTS AND DISCUSSION

Computation Time

First, the computational efficiencies of the proposed method and the conventional DFTB2 were evaluated in terms of CPU time as shown in Figure 1. A default of 60 initial tesserae

per atom was employed in this subsection although this number was increased to 240 for the other calculations in this study.

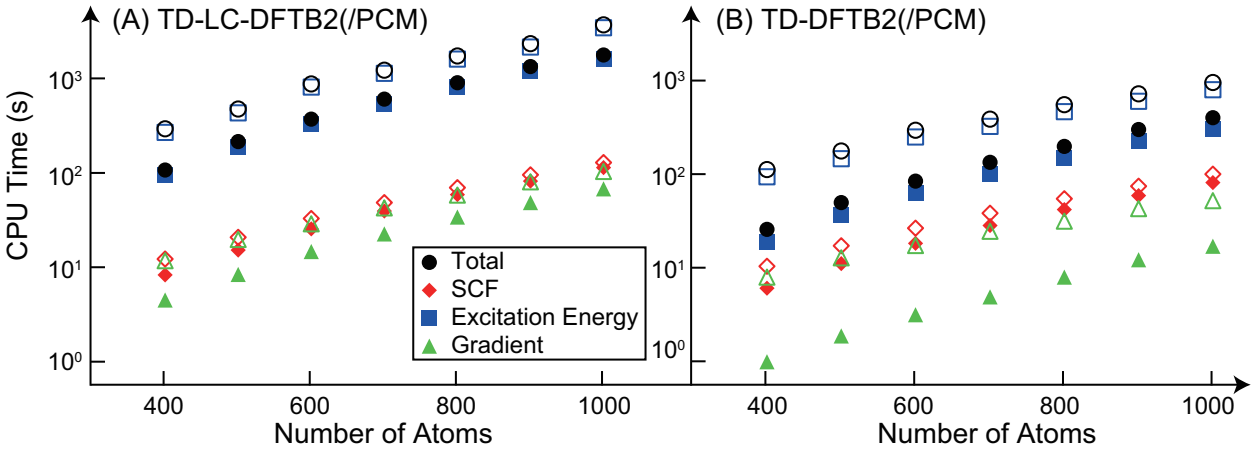

Figure 1: Computation times for (A) TD-LC-DFTB2(/PCM) and (B) TD-DFTB2(/PCM). The total computation time (black square) is broken down into those of the ground-state SCF (red diamond), excitation energy (blue square), and gradient (green triangle) calculation steps. The filled and hollow marks correspond to the times without and with PCM, respectively.

In a vacuum, the observed scalings of the ground-state SCF calculations with LC-DFTB2 and DFTB2 were 2.86 and 2.84 ($\mathcal{O}\left(N_{\mathrm{AO}}^{2.86}\right)$ and $\mathcal{O}\left(N_{\mathrm{AO}}^{2.84}\right)$) , respectively. For the largest system ($n = 10$; 1002 atoms using 2502 basis functions), LC-DFTB2 and DFTB2 took 113.39 and 81.49 s, respectively. Both calculations converged after 13 SCF cycles. However, while the diagonalization of the Hamiltonian matrix took approximately 75 s in both calculations, it took longer to construct the Hamiltonian matrix in LC-DFTB2 (32.5 s) than in DFTB2 (0.3 s); this difference was mainly attributed to the evaluation of the exchange-type contribution in LC-DFTB2 (eq S1 in the Supporting Information). Nevertheless, the diagonalization was more time-consuming than the construction of the Hamiltonian matrix in LC-DFTB2. Comparing the CPU times for the largest system, LC-DFTB2 was only 1.4 times more computationally expensive than the conventional DFTB; this computational cost is small compared to that associated with the integral screening technique, which has been reported to increase the computation time by an order of magnitude.[15] In reality, the efficiency of

algorithms using thresholds depends strongly on the system to be considered, the implementation, and the chosen thresholds. For the present example, a threshold algorithm worked very well because the overlap and density matrices for linear polyacetylene tend to be very sparse. For the largest system, the evaluation of the exchange-type contribution was ten times faster (2.5 s) than the algorithm implemented in this study (32.5 s) with a moderately tight threshold of $\varepsilon = 9$ (see ref 15 for details). Therefore, the 1.4 times increase in the computation time for LC-DFTB2 can be taken as an upper bound. The computation times increased with PCM: LC-DFTB2/PCM and DFTB2/PCM took 128.59 and 99.90 s, respectively. The PCM-related steps (in particular, eq 7) took approximately 2.1 s per SCF cycle; thus, adding PCM contributions was slightly computationally less expensive than adding exchange contributions. For polar systems, however, solving eq 7 may take slightly longer.[11]

Next, the scalings of the excitation energy calculations in a vacuum with TD-LC-DFTB2 and TD-DFTB2 were determined as $\mathcal{O}\left(N_{\mathrm{AO}}^{3.11}\right)$ and $\mathcal{O}\left(N_{\mathrm{AO}}^{3.06}\right)$, respectively, and the CPU times for obtaining the ten lowest excitation energies were 1587.45 and 301.99 s, respectively. Even though LC-DFTB2 was five times more computationally expensive according to this metric, the normalized computation times (obtained by dividing the CPU times by the respective numbers of the trial vectors employed until convergence) for TD-LC-DFTB2 and TD-DFTB2 were 6.78 and 2.46 s, respectively; this indicates that, practically, TD-LC-DFTB2 was 2.76 times more computationally expensive than TD-DFTB2. The major computationally demanding step was the matrix multiplication: DGEMM is called four times per trial vector in the conventional TD-DFTB2 but ten times in TD-LC-DFTB2 (although the dimension is different). Thus, the matrix multiplication in TD-LC-DFTB2 is theoretically 2.5 times more computationally expensive than TD-DFTB2, which is roughly consistent with the observed relative computational cost. With PCM, the CPU time for the largest system was 3448.11 s with TD-LC-DFTB2, which is twice as long as the corresponding calculation time in a vacuum. Further, comparing this time with the normalized CPU time per trial vector (11.27 s) implies that PCM increased the computational cost by

1.7 times. A previous study reported the additional cost due to PCM to be only 10% for the largest system.[11] However, after improving the computational efficiency of solving the TD-DFTB equation (eq 13), solving eq 7 is now relatively time-consuming.

Finally, the scalings of the gradient calculation (including solving the Z-vector equation) with TD-LC-DFTB2 and TD-DFTB2 were $\mathcal{O}\left(N_{\mathrm{AO}}^{2.96}\right)$ and $\mathcal{O}\left(N_{\mathrm{AO}}^{3.12}\right)$, respectively, in a vacuum and 67.60 and 16.99 s, respectively, for the largest system. Solving the Z-vector equation was 1.5–2.0 times more computationally expensive than computing the actual gradient contributions. In both cases, the Z-vector equation converged after three cycles. DGEMM was called several more times in the computation of the gradient contributions in TD-LC-DFTB2 than in TD-DFTB2 (see eq S11 in the Supporting Information) and, as a result, the computation time with TD-LC-DFTB2 was approximately four times longer than that with. For the largest system with PCM, this difference corresponds to an additional computation time of 35 s.

In summary, the LC-DFTB2 calculation for the ground states is approximately 1.4 times more computationally expensive than the conventional DFTB2 with the present implementation. The computation time for the excitation energies depends on the number of matrix–vector products needed to solve the TD-DFTB equation; however if the number of products is roughly the same with both methods, TD-LC-DFTB2 should be approximately 2.5 times more computationally expensive than the conventional DFTB2. Further, the observed scaling is cubic, as expected. Again, no screening thresholds or restriction of the active space were employed in the implemented algorithm. One potential approach to improve the efficiency is to precompute the transition Mulliken population (eq 20) as described in refs 14 and 17; however, this requires a large amount of memory for large molecules.

The memory allocated for the TD-LC-DFTB2 calculation for the largest system was 29 GB. Most of the memory was used for storing trial vectors when solving the TD-DFTB equation. These vectors are stored in replicated memory, so the total memory requirement linearly increases with respect to the number of CPU cores. It is therefore challenging to

perform parallel calculations for very large systems at present. The memory requirement for TD-LC-DFTB2 for the largest system was 246 MB larger than that for the corresponding TD-DFTB2 calculation, which is the actual additional memory that was allocated for TD-LC-DFTB2.

Excited State Intra-Molecular Proton Transfer

3HF absorbs light at a wavelength of 345 nm in ethanol[41] in its ground state (S_0) and emits at wavelengths of 402 or 533 nm in its first excited state (S_1), depending on the position of the proton that is easily transferred at S_1. In a previous study, both TD-DFTB2 and TD-DFTB3 significantly underestimated all of these excitation and emission energies.[11] This is a typical consequence of lack of long-range corrections. As TD-DFT calculations without long-range corrections similarly underestimate excitation and emission energies, it would be interesting to apply TD-LC-DFTB2 with cLR-PCM to the same system. The optimized geometries for TD-DFTB2, TD-DFTB3, and B3LYP/6-31G(d,p) reported in a previous study were used here.

First, the transition structures at S_0 and S_1 were located. Interestingly, LC-DFTB2 at S_0 significantly overestimated the free energy in the transition state (20.11 kcal/mol) relative to the enol form, compared to the corresponding B3LYP/6-31G(d,p) energy (12.17 kcal/mol). Although D3(BJ)[42,43] dispersion corrections could be introduced, as in the parametrization,[38] the relative free energy estimated by LC-DFTB2-D3(BJ) was 20.09 kcal/mol so the effect of the dispersion correction is very small. At S_1, a similar tendency was observed: the free energy in the transition state (5.13 kcal/mol) relative to the enol form significantly deviated from the B3LYP result (1.79 kcal/mol). These observations are not surprising as it has already been reported that LC-DFTB2 is not the most accurate DFTB method for describing potential energy barriers.[38]

The absorption and emission energies that were calculated using the cLR-PCM approach are summarized in Table 1 and those obtained using the standard LR-PCM (most of which

were reported in a previous study[11]) are shown in parentheses. The excitation and emission energies of the enol form that were estimated by TD-LC-DFTB2 were close to those estimated by TD-LC-BLYP/aug-cc-pVDZ. However, it should be noted that both TD-LC-DFTB2 and TD-LC-BLYP/aug-cc-pVDZ provided overestimates compared with the experimentally determined values. Further, the emission energy of the keto form was still significantly underestimated by TD-LC-DFTB2. A similar calculation using the shift and split variants of the OB2 parameter set indicated that the difference of this emission energy was negligibly small: less than 0.01 eV. Notably, the results from B3LYP/6-31G(d,p) with the cLR approach agreed most closely with the experimentally measured values; the largest deviation was only 0.03 eV. Overall, the impact of cLR on the absorption energy estimation was rather small; the difference between LR and cLR was less than 0.1 eV. However, cLR had a larger impact, up to 0.2 eV, on the emission energy estimation. Moreover, the use of the cLR-PCM approach was beneficial with GGA (PBE and BLYP) and hybrid (B3LYP) functionals; however, it increased the deviation when LC-BLYP was employed.

Table 1: Calculated and Experimental[41] Absorption and Emission Energies (in eV). The values outside and inside the parentheses were computed with the cLR-PCM and LR-PCM approaches, respectively.

Method	Absorption	Emission (enol)	Emission (keto)
DFTB2	2.99 (3.02)	2.31 (2.46)	1.34 (1.46)
DFTB3	3.04 (3.04)	2.49 (2.52)	2.00 (1.90)
LC-DFTB2	3.98 (3.92)	3.32 (3.17)	2.04 (1.96)
B3LYP/6-31G(d,p)	3.60 (3.52)	3.11 (2.97)	2.36 (2.17)
B3LYP/aug-cc-pVDZ[a]	3.50 (3.44)	3.06 (2.89)	2.38 (2.20)
PBE/aug-cc-pVDZ[a]	3.10 (3.07)	2.76 (2.62)	2.18 (2.04)
BLYP/aug-cc-pVDZ[a]	3.10 (3.06)	2.75 (2.61)	2.17 (2.03)
LC-BLYP/aug-cc-pVDZ[a]	3.93 (3.86)	3.40 (3.19)	2.52 (2.34)
Experiment	3.59	3.08	2.33

[a] Geometries were optimized at B3LYP/6-31G(d,p)

Benchmark Calculations

Finally, benchmark calculations were performed with the TD-DFTB methods that have been implemented in GAMESS-US so far (namely, TD-DFTB2, TD-DFTB3, and the proposed TD-LC-DFTB2) for a set of molecules collected by Jacquemin et al.[24] The calculated absorption and 0–0 transition energies are summarized in the Supporting Information (Tables S1 and S2); these values are compared with the experimentally derived values in Figure 2. Although the absorption and 0–0 transition energies were computed for 35 and 25 molecules using TD-DFTB2/3 and LC-DFTB2, respectively, only the latter 25 energies were employed in the comparison below. In addition, it was not possible to locate a S_1 minimum of **XVII** (see ref 24) with TD-DFTB3 because there was significant mixing between the excitation vectors in the neighboring states; thus, this molecule was excluded in the comparison of 0–0 transition energies. Therefore, 25 of the absorption energies and 24 of the 0–0 transition energies are plotted in the figure. Furthermore, some optimized geometries in the excited states were identified as transition states (TSs) or even second-order saddle points by vibrational frequency analyzes; while such errors may seem to be unreasonable, a similar phenomenon often occurs with TD-DFT.[28]

Figure 2 (A) shows that TD-LC-DFTB2 overestimated the absorption energies significantly: all of the predicted energies were greater than the corresponding experimental values by at least 0.25 eV Further, the root-mean-square deviation (RMSD) for the 25 molecules was 0.621 eV. TD-DFTB2 and TD-DFTB3 provided better predictions than TD-LC-DFTB2, with RMSDs of 0.384 and 0.386 eV, respectively, for the same 25 molecules. The slope of the line fitted to the estimates obtained by TD-LC-DFTB2 plotted against the experimental values was 0.89, which is closer to 1.00 than those of the other DFTB models (0.80 and 0.78 with TD-DFTB2 and TD-DFTB3, respectively), as summarized in Table 2. However, the intercept of the line that fitted the TD-LC-DFTB2 estimates was as high as 0.91 eV, while those with TD-DFTB2 and TD-DFTB3 were 0.35 and 0.40 eV, respectively; this indicates that the overestimation of the absorption energy with TD-LC-DFTB2 was rather system-

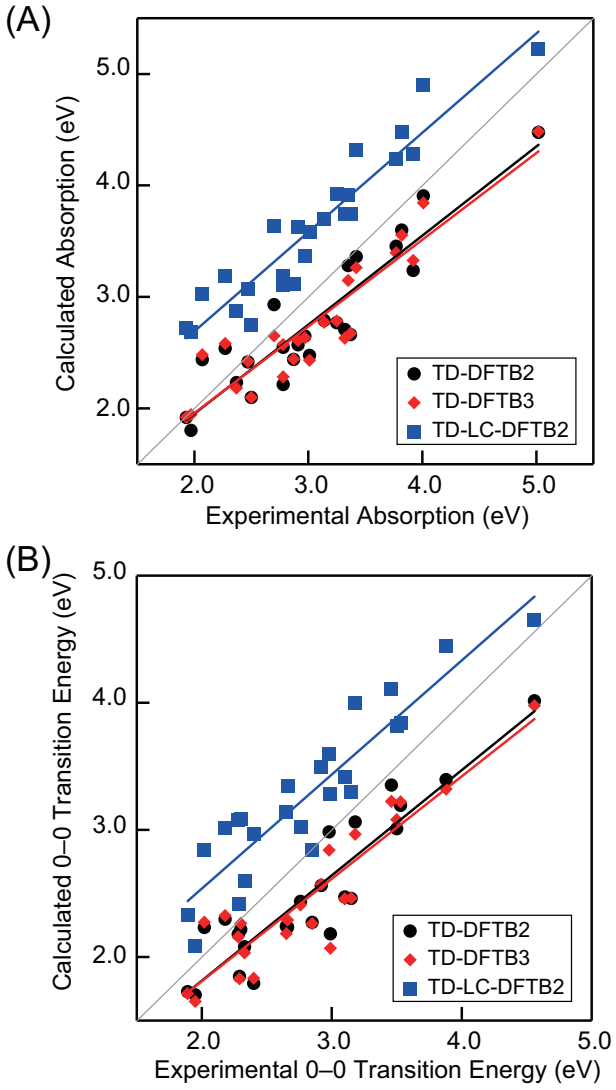

Figure 2: Comparison of experimentally measured and computed (A) absorption energies for 25 molecules and (B) 0–0 transition energies for 24 molecules.

atic. In addition, the R^2 values of the TD-DFTB2, TD-DFTB3, and TD-LC-DFTB2 data were 0.84, 0.86, and 0.90, respectively; thus, the TD-LC-DFTB2 were more closely correlated with the experimental values in comparison to the other methods despite the overestimation. The trend of the predicted 0–0 transition energies (Figure 2 (B)) was similar to that of the absorption energies: TD-LC-DFTB2 overestimated the values but the equation fitted to the data had a slope that was closer to 1.00 than those fitted to the results obtained by the other methods. There is not large difference in the R^2 values.

Table 2: RMSD (in eV), fitted linear equations (FLE)[a], and R^2 values of the absorption energies of 25 molecules and 0–0 transition energies of 24 molecules that were obtained by TD-DFTB2, TD-DFTB3, and TD-LC-DFTB2 compared with the experimental and the CAM-B3LYP results.[24]

		TD-DFTB2	TD-DFTB3	TD-LC-DFTB
		Reference = Experiment		
Absorption	RMSD	0.384	0.386	0.621
	FLE	$y = 0.80x + 0.35$	$y = 0.78x + 0.40$	$y = 0.89x + 0.91$
	R^2	0.84	0.86	0.90
0–0 Transition	RMSD	0.416	0.437	0.522
	FLE	$y = 0.83x + 0.16$	$y = 0.81x + 0.20$	$y = 0.90x + 0.74$
	R^2	0.84	0.84	0.84
		Reference = CAM-B3LYP		
Absorption	RMSD	0.643	0.657	0.250
	FLE	$y = 0.93x - 0.39$	$y = 0.90x - 0.29$	$y = 1.01x + 0.17$
	R^2	0.94	0.95	0.96
0–0 Transition	RMSD	0.637	0.660	0.261
	FLE	$y = 0.94x - 0.42$	$y = 0.91x - 0.35$	$y = 1.06x - 0.00$
	R^2	0.85	0.84	0.92

[a] The fitting linear equation is represented in the form $y = ax + b$, where x is the "Reference" (either experimentally measured energies or those predicted by CAM-B3LYP) and y is the energies computed with TD-DFTB2, TD-DFTB3, or TD-LC-DFTB2.

It should be noted that some of the optimized structures at the excited states are not the minimum structures; even second-order saddle-point structures can be found in some instances. For example, the optimized geometry of **XXXIII** ($C_{16}H_{19}N_2$) was identified as a TS with TD-DFTB2 and TD-DFTB3. The dihedral angle ψ (see Figure 3 (A)) of each of these TSs was nearly 0°. Moreover, the structures were very similar to the optimized

minimum structures predicted by TD-LC-DFTB2 and CAM-B3LYP/6-31G+(d).[24] The true minimum of **XXXIII** on the S_1 potential energy surface was found at $\psi \approx 90°$ using TD-DFTB2 and TD-DFTB3. However, upon inspecting the molecular orbitals and transition vectors, the character of the excitation is a charge-transfer HOMO–LUMO (highest occupied and lowest unoccupied MO) excitation (Figures 3 (B) and (C)) and the resulting equilibrium LR-PCM excitation energies at the minimum were only 0.87 and 0.88 eV with TD-DFTB2 and TD-DFTB3, respectively. The HOMO and LUMO are mostly orthogonal and, therefore, the oscillator strength is trivially small ($< 10^{-5}$). Interestingly, although the excitation energies computed with the equilibrium LR-PCM approach at the minima were positive, the emission energies computed with the non-equilibrium cLR were -1.14 and -1.10 eV, which implies that the excited state after relaxation is more stable than the initial ground state; this is unusual. The cLR free energy at the Kth excited state is computed by[39]

$$\mathcal{G}_K = \mathcal{G}_{\mathrm{GS}} + \Omega_K^{\mathrm{GSRF}} + \frac{1}{2} \sum_{\mu\nu\sigma\kappa\lambda\tau} P^K_{\mu\nu\sigma} G_{\mu\nu,\kappa\lambda} P^K_{\kappa\lambda\tau} \tag{30}$$

where $\mathcal{G}_{\mathrm{GS}}$ is the free energy in the ground state, Ω_K^{GSRF} is the excitation energy in the ground-state reaction field (calculated without $G_{ia\sigma,jb\tau}$ using eqs 14 and 15), and $\mathbf{P}^K$ is the relaxed one-particle difference density matrix for the Kth excited state. The second and third terms are usually positive and negative, respectively, and, in the present case, the value of Ω_K^{GSRF} is so small that the addition of the third term results in a negative emission energy. Exacerbating this issue, non-local (i.e., charge-transfer type) excitation has a greater contribution of the third term than local excitation because the reorganization of the solvent tends to be relatively significant. Although the negative transition energy is unphysical, it can be largely attributed to the fact that the minimum structure is obtained with the equilibrium LR-PCM approach; it may also be an artifact of DFTB without long-range corrections. Adding long-range corrections (i.e., TD-LC-DFTB2) is a practical solution for charge-transfer-type excitation and, indeed, TD-LC-DFTB2 does not exhibit any issues for

this molecule. However, it also predicted a non-minimum structure for another molecule (**XXXV**); thus, the problem remains case dependent.

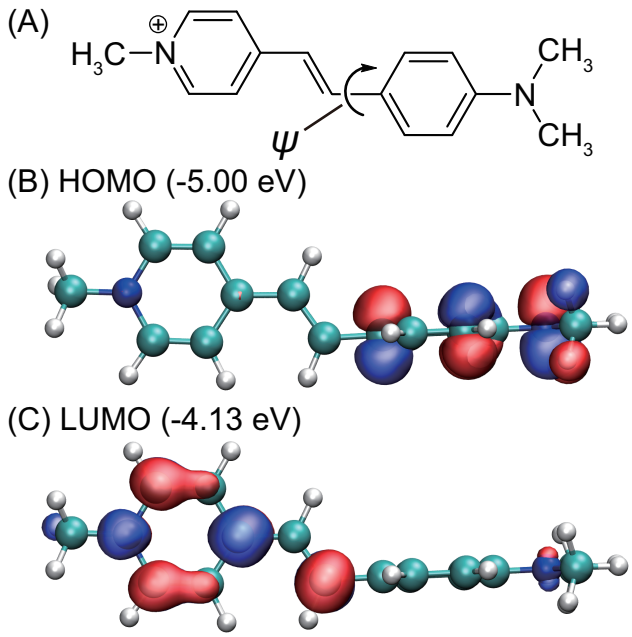

Figure 3: (A) Structure of **XXXIII** and the (B) HOMO and (C) LUMO for the optimized minimum structure on S_1 calculated with DFTB2. The values in parentheses are the eigenvalues (orbital energies) of the HOMO and LUMO.

Comparison with CAM-B3LYP Results

Previous benchmark studies with TD-LC-DFTB2 used CAM-B3LYP[14] and CC3[17] as references; in contrast, experimentally obtained values were used in the previous evaluations. However, in Figure 4, the TD-(LC-)DFTB results (absorption and 0–0 transition energies) obtained by all three methods are further compared with the CAM-B3LYP results reported in ref 24. Interestingly, the absorption and 0–0 transition energies estimated by TD-LC-DFTB2 had RMSDs of 0.250 and 0.261 eV, respectively (see Table 2) when compared with the corresponding CAM-B3LYP results. The slope and intercept of the fitted equations for TD-LC-DFTB2 were closer to 1.00 and 0.00, respectively, than those of the results obtained with other methods; the R^2 value of these results was also high. Hence, although TD-LC-

DFTB2 systematically overestimated the absorption and 0–0 transition energies with respect to the experimentally measured values, they agreed quite well with the CAM-B3LYP results. Considering that DFTB is an approximation of the DFT, DFTB is not expected to be superior to DFT in principle but may offer better results depending on the methods employed during parametrization. The fact that TD-LC-DFTB2 agrees more closely with the CAM-B3LYP results than with the experimentally measured values implies that TD-LC-DFTB2 is an acceptable approximation of the DFT, although a different functional seems to be employed in the derivation of LC-DFTB2 and, possibly, during the parametrization.[15]

These benchmark results imply that TD-LC-DFTB2 can be utilized as a cost-effective approximation of CAM-B3LYP. For instance, the calculation of the absorption energy for a molecule consisting of 22 atoms ($C_{12}H_{10}$; **I**) with CAM-B3LYP/6-31+G(d)/cLR-PCM and LC-DFTB2/cLR-PCM took 58.0 m and 5.6 s, respectively, using one CPU core (Xeon E5-1620 v3). This result implies that LC-DFTB2 is at least two orders of magnitude faster than CAM-B3LYP. It should be kept in mind that TD-LC-DFTB2 often provides higher estimates than CAM-B3LYP; in this benchmark, of the 25 molecules tested, TD-LC-DFTB2 provided higher estimates for 23 of the absorption energies and 21 of the 0–0 transition energies. CAM-B3LYP is also prone to overestimating the absorption and 0–0 transition energies with respect to the experimental values,[24] so those obtained with TD-LC-DFTB2 may be expected to provide even larger overestimation (possibly by 0.5 or 0.6 eV).

Tuning the Range-Separation Parameter

Considering the clear overestimation by LC-DFTB2 but noting its good correlation with long-range corrected DFT, it may be possible to "tune" the range-separation parameter, ω. Decreasing ω value decreases the mixing of the exchange-type contribution, leading to lower transition energies. In principle, the electronic and repulsive parameters have to be parametrized from scratch for each ω because ω is intrinsic to the reference DFT calculation; however, this is rather tedious in practice. Nevertheless, it would be beneficial to investigate

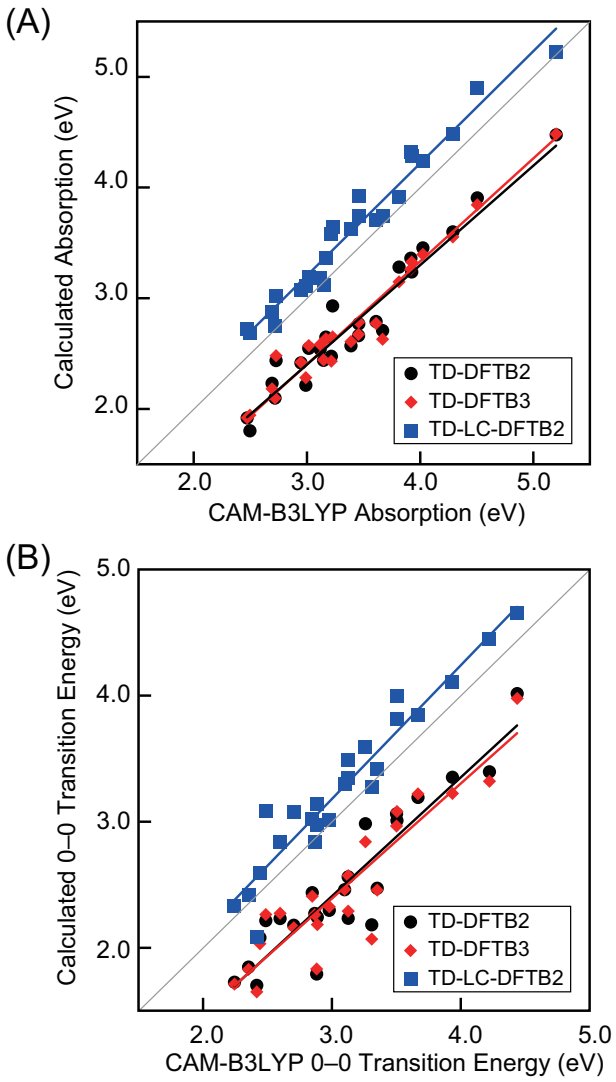

Figure 4: Correlation between the (A) absorption energies for 25 molecules and (B) 0–0 transition energies for 24 molecules calculated with CAM-B3LYP and TD-(LC-)DFTB. The CAM-B3LYP energies were taken from ref 24.

the possible impact of modifying ω in a posteriori manner on the computed properties. Here, in addition to the default $\omega = 0.30$, the same calculations (including the geometry optimizations) were repeated using six lower ω values: 0.25, 0.20, 0.15, 0.10, 0.05, and 0.00.

Table 3 summarizes the computed RMSDs for the absorption and 0–0 transition energies calculated by TD-LC-DFTB2 compared with the experimental and CAM-B3LYP results. The calculated energies (Tables S3 and S4) and the fitted linear equations and R^2 values (Table S5) are provided in the Supporting Information. These results indicate that $\omega = 0.15$ yields the smallest RMSDs (0.134 and 0.172 eV for the absorption and 0–0 transition energies, respectively) for comparison between the TD-LC-DFTB2 and CAM-B3LYP results. However, it should be noted that a lower ω value is akin to predicting the transition structures in the excited state, as noted in Table S4, particularly when the excitation is attributed to a charge-transfer-type excitation. When comparing the TD-LC-DFTB2 results with the experiment results, $\omega = 0.05$ yielded the smallest error; however, the deviation was still as large as 0.373 and 0.295 eV for the absorption and 0–0 transition energies, respectively.

Table 3: RMSDs (in eV) of the TD-LC-DFTB2 absorption (abs) and 0–0 transition energies calculated using different ω values when compared with the experimental and CAM-B3LYP results.

	Reference			
	Experiment		CAM-B3LYP	
ω	abs	0–0	abs	0–0
0.30	0.621	0.522	0.250	0.261
0.25	0.569	0.454	0.202	0.205
0.20	0.496	0.403	0.150	0.178
0.15	0.453	0.344	0.134	0.172
0.10	0.403	0.309	0.154	0.202
0.05	0.373	0.295	0.187	0.248
0.00	0.394	0.312	0.215	0.283

CONCLUSION

In this study, TD-LC-DFTB2 was implemented in conjunction with PCM in GAMESS-US based on an earlier implementation of an LC-DFTB2 method.[22] It was further used to compute excited-state energies and geometries. Analytic first-order derivatives were also implemented by employing the Z-vector method as in the well-known TD-DFT with long-range corrections. The exchange-type term was computed via efficient matrix multiplications and, thus, the scaling of the (TD-)LC-DFTB was expected to be cubic as in the conventional (TD-)DFTB. Compared with the conventional DFTB2, LC-DFTB2 for the ground state was 1.4 times more computationally expensive, while TD-LC-DFTB2 for excited states was approximately three times more computationally expensive. However, a single-point gradient calculation for a system consisting of one thousand atoms took only 30 minutes (without PCM) with one CPU core, demonstrating the advantage of the TD-LC-DFTB2 method. Adding PCM increased the computation time significantly. As a pilot example, in the calculations for 3HF, which exhibits dual emission, TD-LC-DFTB2 predicted similar absorption and enol-form emission energies as TD-LC-BLYP/aug-cc-pVDZ; however, the predicted emission energy of the keto form deviated significantly from experiment and TD-LC-BLYP. Further benchmark calculations were performed using the other TD-DFTB methods implemented in GAMESS-US, TD-DFTB2, TD-DFTB3, and TD-LC-DFTB2, for a set of molecules that was previously collected and theoretically evaluated by Jacquemin et al.[24] Even though TD-LC-DFTB2 clearly overestimated the absorption and 0–0 transition energies when compared with the experimentally measured values, they agreed well with the results obtained by CAM-B3LYP and significantly reduced the computational cost. Further, when the range-separation parameter ω was decreased from 0.30 to 0.15, the results agreed even more closely with CAM-B3LYP. Therefore, based on these benchmark calculations, TD-LC-DFTB2 can be considered a computationally cost-effective approximation of DFT with long-range corrections.

It should be noted that the currently available parameter set[38] is rather limited and only

includes various combinations of H, C, N, and O elements. In addition, the extension to include the third-order Taylor expansion, namely (TD-)LC-DFTB3, is also important. The extension to TD-LC-DFTB3 should be rather straightforward as long as the LC-DFTB3 energy is formulated and appropriate parameters are developed, since TD-DFTB3 has been developed in GAMESS-US.[23] Hence, further development and improvement is essential for practical application studies. The developed method is expected to be publicly available in GAMESS-US in the future.

Acknowledgement

This work was supported by JSPS KAKENHI Grant Number 17K14436.

Supporting Information Available

Implementation details of TD-LC-DFTB2, absorption and 0–0 transition energies calculated with TD-DFTB2, TD-DFTB3, and TD-LC-DFTB2 (Tables S1 and S2), and with TD-LC-DFTB2 using different values of ω (Tables S3 and S4), statistical results of TD-LC-DFTB2 calculations using different values of ω (Table S5), and optimized structures of 3HF with (TD-)LC-DFTB2 and those employed in the benchmark study.

References

(1) Akimov, A. V.; Prezhdo, O. V. Large-Scale Computations in Chemistry: A Bird's Eye View of a Vibrant Field. Cosmic Res. **2015**, 115, 5797–5890.

(2) J., A.; K., F.; K., K. Principles for a Direct SCF Approach to LICAO–MO ab-initio Calculations. J. Comput. Chem. **1982**, 3, 385–399.

(3) Elstner, M.; Porezag, D.; Jungnickel, G.; Elsner, J.; Haugk, M.; Frauenheim, T.;

Suhai, S.; Seifert, G. Self-Consistent-Charge Density-Functional Tight-Binding Method for Simulations of Complex Materials Properties. Phys. Rev. B **1998**, 58, 7260–7268.

(4) Gaus, M.; Cui, Q.; Elstner, M. DFTB3: Extension of the Self-Consistent-Charge Density-Functional Tight-Binding Method (SCC-DFTB). J. Chem. Theory Comput. **2011**, 7, 931–948.

(5) Niehaus, T. A.; Suhai, S.; Della Sala, F.; Lugli, P.; Elstner, M.; Seifert, G.; Frauenheim, T. Tight-Binding Approach to Time-Dependent Density-Functional Response Theory. Phys. Rev. B **2001**, 63, 085108.

(6) Handy, N. C.; Schaefer III, H. F. On the Evaluation of Analytic Energy Derivatives for Correlated Wave Functions. J. Chem. Phys. **1984**, 81, 5031–5033.

(7) Heringer, D.; Niehaus, T. A.; Wanko, M.; Frauenheim, T. Analytical Excited State Forces for the Time-Dependent Density-Functional Tight-Binding Method. J. Comput. Chem. **2007**, 28, 2589–2601.

(8) Wang, F.; Yam, C. Y.; Chen, G.; Wang, X.; Fan, K.; Niehaus, T. A.; Frauenheim, T. Linear Scaling Time-Dependent Density-Functional Tight-Binding Method for Absorption Spectra of Large Systems. Phys. Rev. B **2007**, 76, 045114.

(9) Fan, G.-H.; Han, K.-l.; He, G.-Z. Time- dependent Density Functional- based Tight - bind Method Efficiently Implemented with OpenMP Parallel and GPU Acceleration. Chin. J. Chem. Phys. **2013**, 26, 635–645.

(10) Rüger, R.; van Lenthe, E.; Lu, Y.; Frenzel, J.; Heine, T.; Visscher, L. Efficient Calculation of Electronic Absorption Spectra by Means of Intensity-Selected Time-Dependent Density Functional Tight Binding. J. Chem. Theory Comput. **2015**, 11, 157–167.

(11) Nishimoto, Y. DFTB/PCM Applied to Ground and Excited State Potential Energy Surfaces. J. Phys. Chem. A **2016**, 120, 771–784.

(12) Alkan, F.; Aikens, C. M. TD-DFT and TD-DFTB Investigation of the Optical Properties and Electronic Structure of Silver Nanorods and Nanorod Dimers. J. Phys. Chem. C **2018**, 122, 23639–23650.

(13) Niehaus, T. A.; Della Sala, F. Range Separated Functionals in the Density Functional Based Tight-Binding Method: Formalism. Phys. Status Solidi B **2012**, 249, 237–244.

(14) Humeniuk, A.; Mitrić, R. Long-Range Correction for Tight-Binding TD-DFT. J. Chem. Phys. **2015**, 143, 134120.

(15) Lutsker, V.; Aradi, B.; Niehaus, T. A. Implementation and Benchmark of a Long-Range Corrected Functional in the Density Functional Based Tight-Binding Method. J. Chem. Phys. **2015**, 143, 184107.

(16) Humeniuk, A.; Mitrić, R. DFTBaby: A Software Package for Non-Adiabatic Molecular Dynamics Simulations Based on Long-Range Corrected Tight-Binding TD-DFT(B). Comput. Phys. Commun. **2017**, 221, 174 – 202.

(17) Kranz, J. J.; Elstner, M.; Aradi, B.; Frauenheim, T.; Lutsker, V.; Garcia, A. D.; Niehaus, T. A. Time-Dependent Extension of the Long-Range Corrected Density Functional Based Tight-Binding Method. J. Chem. Theory Comput. **2017**, 13, 1737–1747.

(18) Stojanović, L.; Aziz, S. G.; Hilal, R. H.; Plasser, F.; Niehaus, T. A.; Barbatti, M. Nonadiabatic Dynamics of Cycloparaphenylenes with TD-DFTB Surface Hopping. J. Chem. Theory Comput. **2017**, 13, 5846–5860.

(19) Tomasi, J.; Mennucci, B.; Cammi, R. Quantum Mechanical Continuum Solvation Models. Chem. Rev. **2005**, 105, 2999–3094.

(20) Barone, V.; Carnimeo, I.; Scalmani, G. Computational Spectroscopy of Large Systems in Solution: The DFTB/PCM and TD-DFTB/PCM Approach. J. Chem. Theory Comput. **2013**, 9, 2052–2071.

(21) Schmidt, M. W.; Baldridge, K. K.; Boatz, J. A.; Elbert, S. T.; Gordon, M. S.; Jensen, J. H.; Koseki, S.; Matsunaga, N.; Nguyen, K. A.; Su, S. et al. General Atomic and Molecular Electronic Structure System. J. Comput. Chem. **1993**, 14, 1347–1363.

(22) Vuong, V. Q.; Nishimoto, Y.; Fedorov, D. G.; Sumpter, B. G.; Niehaus, T. A.; Irle, S. The Fragment Molecular Orbital Method Based on Long-Range Corrected Density-Functional Tight-Binding. J. Chem. Theory Comput. **2019**, 15, 3008–3020.

(23) Nishimoto, Y. Time-Dependent Density-Functional Tight-Binding Method with the Third-Order Expansion of Electron Density. J. Chem. Phys. **2015**, 143, 094108.

(24) Jacquemin, D.; Planchat, A.; Adamo, C.; Mennucci, B. TD-DFT Assessment of Functionals for Optical 0-0 Transitions in Solvated Dyes. J. Chem. Theory Comput. **2012**, 8, 2359–2372.

(25) Parr, R. G.; Pearson, R. G. Absolute Hardness: Companion Parameter to Absolute Electronegativity. J. Am. Chem. Soc. **1983**, 105, 7512–7516.

(26) Barone, V.; Cossi, M. Quantum Calculation of Molecular Energies and Energy Gradients in Solution by a Conductor Solvent Model. J. Phys. Chem. A **1998**, 102, 1995–2001.

(27) Weiss, H.; Ahlrichs, R.; Häser, M. A Direct Algorithm for Self-Consistent-Field Linear Response Theory and Application to C_{60}: Excitation Energies, Oscillator Strengths, and Frequency-Dependent Polarizabilities. J. Chem. Phys. **1993**, 99, 1262–1270.

(28) Furche, F.; Ahlrichs, R. Adiabatic Time-Dependent Density Functional Methods for Excited State Properties. J. Chem. Phys. **2002**, 117, 7433–7447.

(29) Scalmani, G.; Frisch, M. J.; Mennucci, B.; Tomasi, J.; Cammi, R.; Barone, V. Geometries and Properties of Excited States in the Gas Phase and in Solution: Theory and Application of a Time-Dependent Density Functional Theory Polarizable Continuum Model. J. Chem. Phys. **2006**, 124, 094107.

(30) Wang, Y.; Li, H. Excited State Geometry of Photoactive Yellow Protein Chromophore: A Combined Conductorlike Polarizable Continuum Model and Time-Dependent Density Functional Study. J. Chem. Phys. **2010**, 133, 034108.

(31) Chiba, M.; Tsuneda, T.; Hirao, K. Excited State Geometry Optimizations by Analytical Energy Gradient of Long-Range Corrected Time-Dependent Density Functional Theory. J. Chem. Phys. **2006**, 124, 144106.

(32) Hirata, S.; Head-Gordon, M. Time-Dependent Density Functional Theory within the Tamm–Dancoff Approximation. Chem. Phys. Lett. **1999**, 314, 291 – 299.

(33) Niehaus, T.; Elstner, M.; Frauenheim, T.; Suhai, S. Application of an Approximate Density-Functional Method to Sulfur Containing Compounds. J. Mol. Struct.: THEOCHEM **2001**, 541, 185–194.

(34) Kubař, T.; Bodrog, Z.; Gaus, M.; Köhler, C.; Aradi, B.; Frauenheim, T.; Elstner, M. Parametrization of the SCC-DFTB Method for Halogens. J. Chem. Theory Comput. **2013**, 9, 2939–2949.

(35) Gaus, M.; Goez, A.; Elstner, M. Parametrization and Benchmark of DFTB3 for Organic Molecules. J. Chem. Theory Comput. **2013**, 9, 338–354.

(36) Gaus, M.; Cui, Q.; Elstner, M. Density Functional Tight Binding: Application to Organic and Biological Molecules. WIREs Comput. Mol. Sci. **2014**, 4, 49–61.

(37) Kubillus, M.; Kubař, T.; Gaus, M.; Řezáč, J.; Elstner, M. Parameterization of the DFTB3 Method for Br, Ca, Cl, F, I, K, and Na in Organic and Biological Systems. J. Chem. Theory Comput. **2015**, 11, 332–342.

(38) Vuong, V. Q.; Akkarapattiakal Kuriappan, J.; Kubillus, M.; Kranz, J. J.; Mast, T.; Niehaus, T. A.; Irle, S.; Elstner, M. Parametrization and Benchmark of Long-Range Corrected DFTB2 for Organic Molecules. J. Chem. Theory Comput. **2018**, 14, 115–125.

(39) Caricato, M.; Mennucci, B.; Tomasi, J.; Ingrosso, F.; Cammi, R.; Corni, S.; Scalmani, G. Formation and Relaxation of Excited States in Solution: A New Time Dependent Polarizable Continuum Model Based on Time Dependent Density Functional Theory. J. Chem. Phys. **2006**, 124, 124520.

(40) Cammi, R.; Corni, S.; Mennucci, B.; Tomasi, J. Electronic Excitation Energies of Molecules in Solution: State Specific and Linear Response Methods for Nonequilibrium Continuum Solvation Models. J. Chem. Phys. **2005**, 122, 104513.

(41) Ameer-Beg, S.; Ormson, S. M.; Brown, R. G.; Matousek, P.; Towrie, M.; Nibbering, E. T. J.; Foggi, P.; Neuwahl, F. V. R. Ultrafast Measurements of Excited State Intramolecular Proton Transfer (ESIPT) in Room Temperature Solutions of 3-Hydroxyflavone and Derivatives. J. Phys. Chem. A **2001**, 105, 3709–3718.

(42) Grimme, S.; Antony, J.; Ehrlich, S.; Krieg, H. A Consistent and Accurate Ab Initio Parametrization of Density Functional Dispersion Correction (DFT-D) for the 94 Elements H-Pu. J. Chem. Phys. **2010**, 132, 154104.

(43) Grimme, S.; Ehrlich, S.; Goerigk, L. Effect of the Damping Function in Dispersion Corrected Density Functional Theory. J. Comput. Chem. **2011**, 32, 1456–1465.

Graphical TOC Entry